Nucleic Acids Research, 2025, **53**, gkaf610
https://doi.org/10.1093/nar/gkaf610
Molecular and Structural Biology

Antitoxin control of optimal transcriptional repression in the atypical HigB–HigA toxin–antitoxin system from *Proteus vulgaris*

Ian J. Pavelich[1], Marc A. Schureck[1,2], Pooja Srinivas[1,3], Taylor M. Blackburn[1], Dongxue Wang[1], Eric D. Hoffer[1,2], Michelle Boamah[1], Kimberly Zaldana[1], Nina Onuoha[1], Stacey J. Miles[1], Marcin Grabowicz[4,5], C. Denise Okafor[6], Christine M. Dunham[1,*]

[1]Department of Chemistry and the Emory Antibiotic Resistance Center, Emory University, Atlanta, GA 30322, United States
[2]Biochemistry, Cell and Developmental Biology Graduate Program, Emory University, Atlanta, GA 30322, United States
[3]Molecular and Systems Pharmacology Graduate Program, Emory University, Atlanta, GA 30322, United States
[4]Department of Microbiology and Immunology, Emory University School of Medicine, Atlanta, GA 30322, United States
[5]Division of Infectious Diseases, Department of Medicine, Emory University School of Medicine, Atlanta, GA 30322, United States
[6]Department of Biochemistry and Molecular Biology, Pennsylvania State University, University Park, PA 16802, United States
[*]To whom correspondence should be addressed. Email: christine.m.dunham@emory.edu

Abstract

Bacterial toxin–antitoxin (TA) pairs transcriptionally autoregulate their expression via a repression/derepression mechanism in response to changing environmental conditions. The structural diversity of TA systems influences the mechanisms of transcriptional regulation. Here, we define the molecular mechanism for the plasmid-encoded HigB–HigA TA pair originally identified in a post-operative infection with antibiotic-resistant *Proteus vulgaris*. We determine DNA binding and promoter activity by the HigB–HigA complex supported by structural biology and molecular dynamics simulations of an elusive DNA operator–TA repressor complex. To define the optimal oligomeric TA repressor–DNA operator complex required for derepression, we engineered a dedicated trimeric HigB–$HigA_2$ complex that represses transcription more than 26-fold as compared to the tetrameric $HigB_2$–$HigA_2$. These results expand the known diversity of how the HigB–HigA TA family is autoregulated.

Graphical abstract

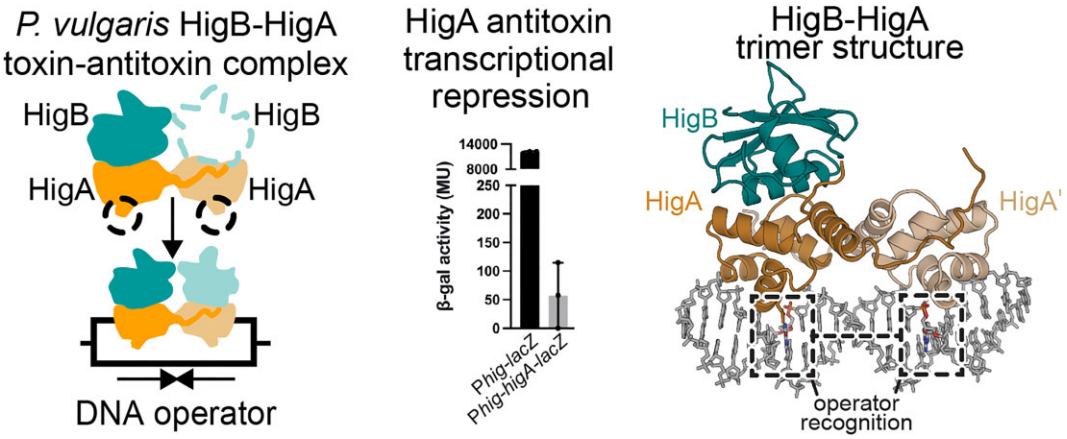

Introduction

Bacterial toxin–antitoxin (TA) modules are two-component systems arranged in bicistronic operons. TAs were originally found on plasmids and subsequently found in bacteriophages and on the chromosomes of bacteria [1–9]. There are now eight different types of TA systems classified by the characteristics of the antitoxin [10]. In the past few decades, conflicting data regarding the endogenous roles of TAs have led to ambiguity and controversy surrounding their functions in bacterial physiology [11]. Despite this, we know that TAs are

Received: September 30, 2024. **Revised:** May 21, 2025. **Editorial Decision:** June 5, 2025. **Accepted:** June 23, 2025

activated during diverse environmental cues, and more recently, they have been implicated in phage resistance and bacterial immunity [12–14].

Type II TAs are the most abundant and best-studied systems with both the toxin and antitoxin being proteinaceous. Antitoxins are generally more labile and need continued expression to suppress cognate toxin partners and thus prevent toxin action, which is generally inhibition of a cellular process [15–17]. Expression is autoregulated at the transcriptional level via a negative feedback loop [11, 18]. Antitoxin proteins contain both a toxin binding domain and a DNA-binding motif and bind at DNA operator sequences that overlap with the promoters of TA genes to repress transcription. While both the TA complex and the antitoxin alone can bind at operator sites, toxin binding usually results in greater transcriptional repression. Transcription is then tuned to changes in toxin:antitoxin ratios bound at DNA operators, which results in a response called conditional cooperativity [19–23]. In this mechanism, toxin binding is enhanced at low molar levels of the TA–DNA repressor complex. When toxin levels increase and achieve a greater than 1:1 molar stoichiometry with the antitoxin bound at the DNA operator, the toxin switches from a transcriptional co-repressor to a derepressor. However, the mechanism of conditional cooperativity does not seem to describe how all type II TAs are transcriptionally regulated and these outliers include *Escherichia coli* MqsR–MqsA, *E. coli* HicA–HicB, and *E. coli* DinJ–YafQ [24–27].

The structural diversity and distinct toxin- and DNA-binding motifs of different type II antitoxin proteins may partially explain why they can exert different regulatory mechanisms [18]. Antitoxins contain ribbon–helix–helix (RHH), helix–turn–helix (HTH), Phd/YefM, or SpoVT/AbrB DNA-binding motifs, with RHH and HTH being the most common [26, 28–33]. The type of DNA-binding motif affects transcriptional repression and directly affects the oligomeric state of the TA–DNA repressor complex. HTH-containing antitoxins contain a complete DNA-binding motif, while RHH-containing antitoxins contain only a half site requiring antitoxin dimerization to bind to the DNA repressor site (Fig. 1). TAs usually contain multiple repressor operator sites and antitoxin binding at adjacent sites can lead to cooperativity and an increase in transcriptional repression [21–23, 34]. Since antitoxins are labile and susceptible to proteases especially during changing cellular conditions [35], the reduction in antitoxin concentration increases the level of free toxin that, in turn, inhibits growth. Free toxin can also interact with antitoxins bound at their operators in the context of the DNA–TA repressor complex changing the TA ratio and resulting in an increase in transcription. In TA systems that are regulated by conditional cooperativity, higher oligomeric TA–DNA repressor complexes lead to greater affinity for the DNA operator and directly influence transcriptional repression as seen in the CcdB–CcdA, RelB–RelE, Phd–Doc, and TacA–TacT systems [21–23, 30]. In the other TAs not regulated by conditional cooperativity, like the HicB–HicA, MqsR–MqsA, and GraT–GraA systems, toxin binding to either the antitoxin or the DNA repressor complex is mutually exclusive and antitoxin binding to the DNA operator solely functions as a derepressor [24, 27, 36]. Alternatively, other TA systems appear to function as simple on/off transcriptional switches (e.g., DinJ–YafQ) [25]. While there exists some experimental evidence that distinguishes between these modes of regulation, the molecular basis for each mechanism is ambiguous because there is little or no structural evidence to support changing TA molar ratios as a foundation for the conditional cooperativity model.

The *host inhibition of growth* BA (*higBhigA*) TA module was first identified on the antibiotic-resistance plasmid Rts1 associated with *Proteus vulgaris* and discovered postoperatively in an urinary tract infection [37, 38] (this TA pair is called "HigB–HigA" to denote both the HigB toxin and HigA antitoxin proteins). The HigB toxin belongs to the RelE family of toxins, resembles a microbial ribonuclease, and cleaves mRNA substrates bound to a translating ribosome [26, 39–42]. The HigB–HigA family is also found chromosomally, and in *E. coli, Pseudomonas putida* (called GraTGraA), and *Vibrio cholerae*, these HigB toxins are also RelE family members [36, 43–46]. However, the structural organization and the regulation of these systems as compared to the *P. vulgaris* TA module are different [26]. For example, while all four HigA homologs contain an HTH DNA-binding motif, the *P. vulgaris* antitoxin binds to each of its two operator sites (O1 and O2) in a noncooperative manner distinct from *E. coli* and *P. putida* HigA [26, 46–47]. Further, *V. cholerae* HigA2 antitoxin contains an intrinsically disordered region found to be important for binding to operator DNA. These different mechanisms, even among HigB–HigA homologs, speak to the diversity in mechanisms among TAs.

Here, we determined that addition of *P. vulgaris* HigB toxin does not increase transcriptional repression and, in fact, the HigA antitoxin alone robustly represses transcription. Despite this, excess HigB can still cause derepression of the HigB–HigA●*hig* DNA complex. Structures of the HigB–HigA●*hig* DNA repressor complex reveal that HigB–HigA can adopt either trimeric HigB–$HigA_2$ or tetrameric $HigB_2$–$HigA_2$ forms. Engineered trimeric HigB–$HigA_2$ can still bind *hig* and represses transcription >26-fold more than tetrameric $HigB_2$–$HigA_2$. These results provide insights into an atypical TA system and reveal different mechanisms even within HigB–HigA homologs.

Materials and methods

Strains and plasmids

E. coli BL21(DE3) were used for expression of His_6-HigA, His_6-HigB–HigA, and HigB–HigA-His_6 proteins from pET28a, pET28a, and pET21c vectors, respectively, as previously reported [26]. *E. coli* BW25113 were used for all β-galactosidase (β-gal) experiments and HigB(H54A)-His_6 expression [48]. All point mutations were introduced by site-directed mutagenesis and sequences were verified by DNA sequencing (Azenta).

HigA, HigB, and HigB–HigA purification

The His_6-HigA, His_6-HigB–HigA, and HigB–HigA-His_6 protein complexes were overexpressed and purified as previously described with minor modifications [26]. These differences included expression of His_6-HigA at 18°C overnight after protein induction and removal of the His_6 tag from His_6-HigA and His_6-HigB–HigA with thrombin prior to gel filtration chromatography. HigB(H54A) protein was overexpressed and purified as previously described [49].

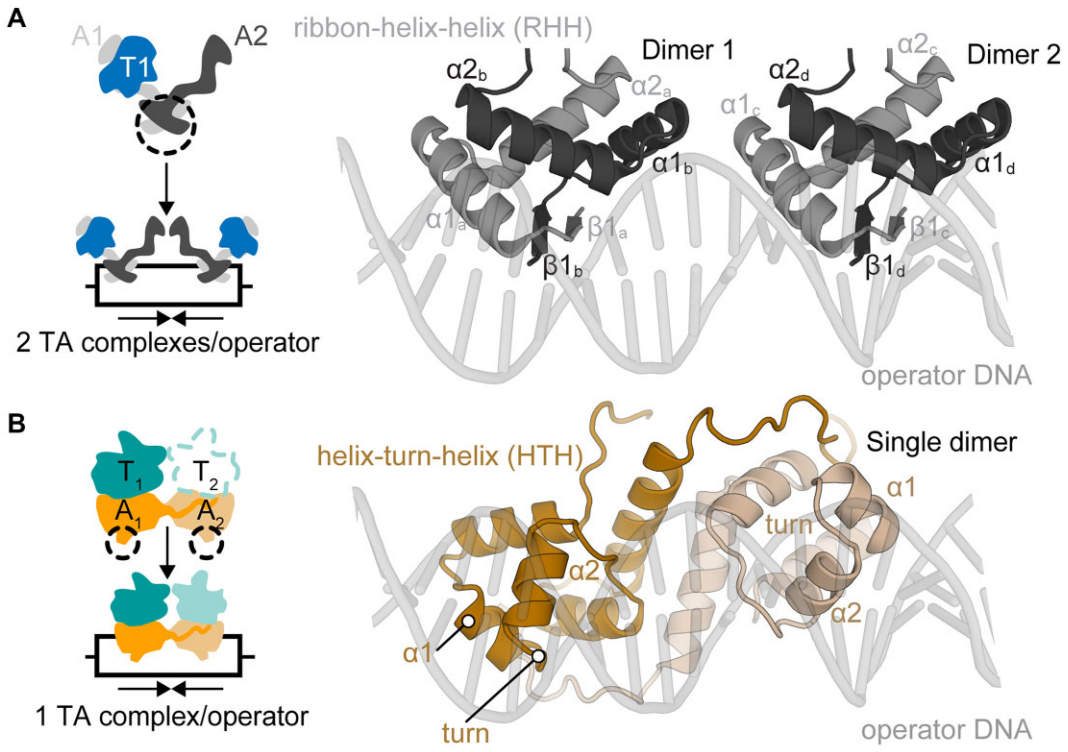

Figure 1. Diverse transcriptional control mechanisms that regulate expression of Type II TA complexes. Toxin (T) and antitoxin (A) proteins form multimeric complexes that bind operator sites (O1 and O2) that overlap with their promoters (P_{TA}) to repress transcription using different DNA-binding domains (black dotted circles). (**A**) Ribbon–helix–helix DNA-binding motifs form a half-site, requiring antitoxin dimerization to form a single complete DNA-binding motif. (**B**) In contrast, other antitoxins that contain a helix–turn–helix DNA- binding motif are a complete DNA-binding motif and do not require dimerization for DNA binding.

Electrophoretic mobility shift assays

To construct the dsDNA for the electrophoretic mobility shift assays (EMSA), pairs of complementary single-stranded oligonucleotides were diluted to 2 μM each in DNA buffer (100 mM NaCl, 10 mM Tris–HCl, pH 8). The O1–O2, O1–O2(scrambled), O1(scrambled)–O2, and O1(scrambled)–O2(scrambled) oligonucleotide mixtures of the *hig* promoter fragment were incubated in boiling water and then cooled at room temperature overnight (Supplementary Table S1). The dsDNA oligos were diluted to 150 nM in EMSA binding buffer (100 mM NaCl, 10 mM $MgCl_2$, 5% glycerol, 0.01 mg/ml bovine serum albumin). Purified wild-type HigB–HigA protein was diluted to 10 μM in EMSA binding buffer and serially diluted to give a series of protein concentrations ranging from 0 to 600 nM. The binding reactions were incubated at room temperature for 20 min and 10 μl of each reaction was loaded onto 8% native, polyacrylamide–0.5× TBE/10% glycerol gels (50 mM Tris–HCl, pH 8, 50 mM boric acid, 5 mM EDTA, 10% glycerol) and subjected to electrophoresis at 110 V limiting at 4°C for 120 min. To visualize the DNA and DNA–protein complexes, the gels were stained with SYBR Green stain (Thermo Fisher Scientific) in 0.5× TBE/10% glycerol for 30 min with gentle agitation and then the fluorescence was imaged with a Typhoon Trio phosphoimager (GE Healthcare; 488 nm excitation and 526 nm emission). Assays were performed in duplicate with representative gels shown. Band intensities for both free and bound *hig* DNA were quantified with ImageQuant 1D gel analysis software using the rolling ball background subtraction. For HigB–HigA bound to either O1 or O2, the binding data were fit using a one site-specific binding equation [Y (specific binding, μM) = $B_{max} \times X/(K_d + X)$] in GraphPad Prism 9.0.0.

Reporter assays

For the β-gal activity assays testing binding of HigB–HigA to the *hig* O1 or O2 DNA sites, the *hig* operator was chemically synthesized (IDT), digested, and ligated into a pQF50 vector with *lacZ* downstream (pQF50-P*hig* or pQF50-P*hig-higA*). *E. coli* BW25113 transformed with pQF50-*hig* mutants were used for all experiments. Activity in Miller units (MUs) was measured using the following formula: total activity (MU) = $(1000 \times OD_{420})/[OD_{600} \times$ volume of culture used (ml) $\times$ 0.5]. Assays were performed in triplicate with two technical replicates. Error bars represent the mean ± SD of values from three independent experiments performed in technical replicates (raw values shown as individual points).

For the β-gal activity assays where *E. coli* BW25113 was transformed with pOU254-P*hig* and pOU254-P*hig-higBhigA*, pOU254-P*hig-higB*(L5ext)*higA*, or pBAD33-*higB*(H54A), *hig* was chemically synthesized (IDT), digested, and ligated into a pOU254 vector with *lacZ* downstream as previously used for RelB–RelE studies [22]. *E. coli* BW25113 transformed with pOU254-*hig* variants or pBAD33-*higB*(H54A) were used for all experiments. The β-gal activity assays in the absence or presence of HigB(H54A) were performed using a previously described method [47] and activity was measured similarly as described above.

Crystallization, data collection, and structure determination of the HigB–HigA•*hig* O2 DNA complexes

The complex was formed by mixing either His_6-HigB–HigA or selenomethionine-derivatized HigB–HigA-His_6 (both in 40 mM Tris–HCl, pH 7.5, 250 mM KCl, 5 mM $MgCl_2$, and 5 mM β-mercaptoethanol) with O2 DNA (10 mM Tris, pH 8, 100 mM NaCl, and 1 mM EDTA) at one $HigB_2$–$HigA_2$ tetramer to one O2 dsDNA molar ratio. The complexes were diluted to 5.95 mg/ml HigB–HigA and 1.55 mg/ml O2 DNA by the addition of buffer (20 mM Tris–HCl, pH 8, 10 mM $MgCl_2$, and 100 mM NaCl). Crystals of HigB–HigA bound to O2 DNA were grown by sitting drop vapor diffusion and crystallized in 0.2 M $CaCl_2$ and 10%–25% (w/v) polyethylene glycol 3350 at 20°C. Both crystal forms grew after 2 days and were cryoprotected by serially increasing the concentration of ethylene glycol in the mother liquor from 10–30% (w/v) followed by flash freezing in liquid nitrogen.

Two X-ray datasets were collected at the Northeastern Collaborative Access Team (NE-CAT) 24-ID-C and Southeast Regional Collaborative Access Team (SER-CAT) 22-ID facilities at the Advanced Photon Source (APS) at the Argonne National Laboratory. For the tetrameric $HigB_2HigA_2$•*hig* O2 complex, 360° data (0.5° oscillations) were collected on a PILATUS 6M-F detector (DECTRIS Ltd, Switzerland) using 0.9792 Å radiation. For the trimeric HigB–$HigA_2$•*hig* O2 complex, 90° data (0.5° oscillations) were collected on a MARMOSAIC 300-mm CCD detector (Rayonix, LLC, USA) using 1.0 Å radiation. XDS was used to integrate and scale the data [50]. The tetrameric $HigB_2$–$HigA_2$•*hig* O2 structure was solved by single wavelength anomalous diffraction phasing using AutoSol from the PHENIX software suite [51] and 13 heavy atom sites were found. The trimeric HigB–$HigA_2$•*hig* O2 structure was solved using the structure of the $HigA_2$ dimer (PDB code 6CF1) as a molecular replacement search model in the PHENIX software suite. XYZ coordinates, real space, and *B*-factors (isotropic) were refined iteratively in PHENIX and model building was performed using the program Coot [52]. Final refinement of the structures gave crystallographic R_{work}/R_{free} of 17.6/21.8% for trimeric HigB–$HigA_2$•*hig* O2 and 17.5/22.1% for tetrameric $HigB_2$–$HigA_2$•*hig* O2. All figures were created in PyMol.

Dianthus binding assays

To determine the affinity of HigB–HigA binding when both operators are available, we monitored the change in fluorescence of a 12.5 nM Cy5-labeled *hig* DNA operator (in EMSA binding buffer) upon the addition of increasing amounts of HigB–HigA. Purified wild-type HigB–HigA was diluted to 325 nM in EMSA binding buffer and serially diluted to give a series of protein concentrations ranging from 50 to 325 nM. Reactions were incubated on ice for 10 min. Fluorescence was measured using a Dianthus NT.23 Pico (NanoTemper Technologies) instrument. Fluorescence values were baseline corrected and plotted against HigB–HigA concentration. Data from three independent measurements were fit using a specific binding equation with Hill coefficient equation [Y (specific binding) = $B_{max} \times X^h/(K_d{}^h + X^h)$; h = Hill coefficient] in GraphPad Prism 9.0.0.

Differential scanning fluorimetry

The thermal stabilities of wild-type HigB–HigA and HigB(L5ext)–HigA were assessed using a Tycho NT.6 instrument (NanoTemper). Protein was heated at 0.1°C steps over a temperature range of 35–95°C, during which intrinsic fluorescence at 350 and 330 nm was measured. Inflection temperature (T_i) was determined for each apparent unfolding transition from the temperature-dependent change in the ratio of 350 and 330 nm measurements. Assays were performed in triplicates.

Molecular dynamics simulations

Starting models for molecular dynamics (MD) simulations were prepared from PDB codes 6W6U ($HigB_2$–$HigA_2$•*hig* O2) and 6WFP (HigB–$HigA_2$•*hig* O2). Simulations were performed on the tetrameric or trimeric HigB–HigA structures in the absence or presence of O2 DNA ($HigB_2$–$HigA_2$•*hig* O2, HigB–$HigA_2$•*hig* O2, $HigB_2$–$HigA_2$, and HigB–$HigA_2$). All complexes were prepared using the Xleap module of AmberTools 18 [53], the ff14SB forcefield for protein atoms, [54] and the OL15 forcefield [55] for DNA. Complexes were solvated in an octahedral box of TIP3P water [56] with a 10 Å buffer. Ions were added to each complex to achieve a final concentration of 150 mM NaCl. Minimization was performed in three rounds, each employing steepest descent (5000 steps) followed by conjugate gradient (5000 steps). In the first round, restraints of 500 kcal/(mol Å^2) were applied to all solute atoms. In the second round, solute restraints were reduced to 100 kcal/(mol Å^2). All restraints were removed in the third round. Complexes were heated from 0 to 300 K with a 100-ps run with constant volume periodic boundaries and restraints of 10 kcal/(mol Å^2) on solute atoms. All MD simulations were performed using AMBER2018 [53, 57, 58]. Two stages of equilibration were performed: 10-ns MD in the NPT ensemble with 10 kcal/(mol Å^2) restraints on solute atoms, followed by an additional 10-ns MD run with restraints reduced to 1 kcal/(mol Å^2). Finally, all restraints were removed and 1-μs production simulations obtained for each complex. Long-range electrostatics were evaluated with a cutoff of 10 Å and all heavy atom–hydrogen bonds were fixed with the SHAKE algorithm [59]. Following MD, the CPPTRAJ module [60] of AmberTools 18 was used to calculate root mean square fluctuations (RMSFs) of each protein residue in each complex.

Results

Independent HigB–HigA recognition of DNA repressor O1 site or O2 site

The *hig* promoter (P*hig*) is repressed by the HigB–HigA complex binding at operators O1 and O2 that overlap with its −35 and −10 sites and prevent RNA polymerase from gaining access to the promoter [38] (Fig. 2A). We previously determined the binding affinities of both HigA and HigB–HigA to *hig* O1 or O2 [47]. In these studies, we used a 21-bp dsDNA that contained either *hig* O1 or O2. HigA antitoxin binds to either *hig* O1 or O2 with a similar affinity (0.14 ± 0.03 or 0.13 ± 0.03 μM, respectively) and HigB–HigA binds to either *hig* O1 or O2 with a two-fold lower affinity (0.36 ± 0.10 or 0.24 ± 0.04 μM, respectively). We next sought to determine whether the binding of HigB–HigA at its operators is cooperative. We monitored HigB–HigA binding to *hig* O1 or O2 using

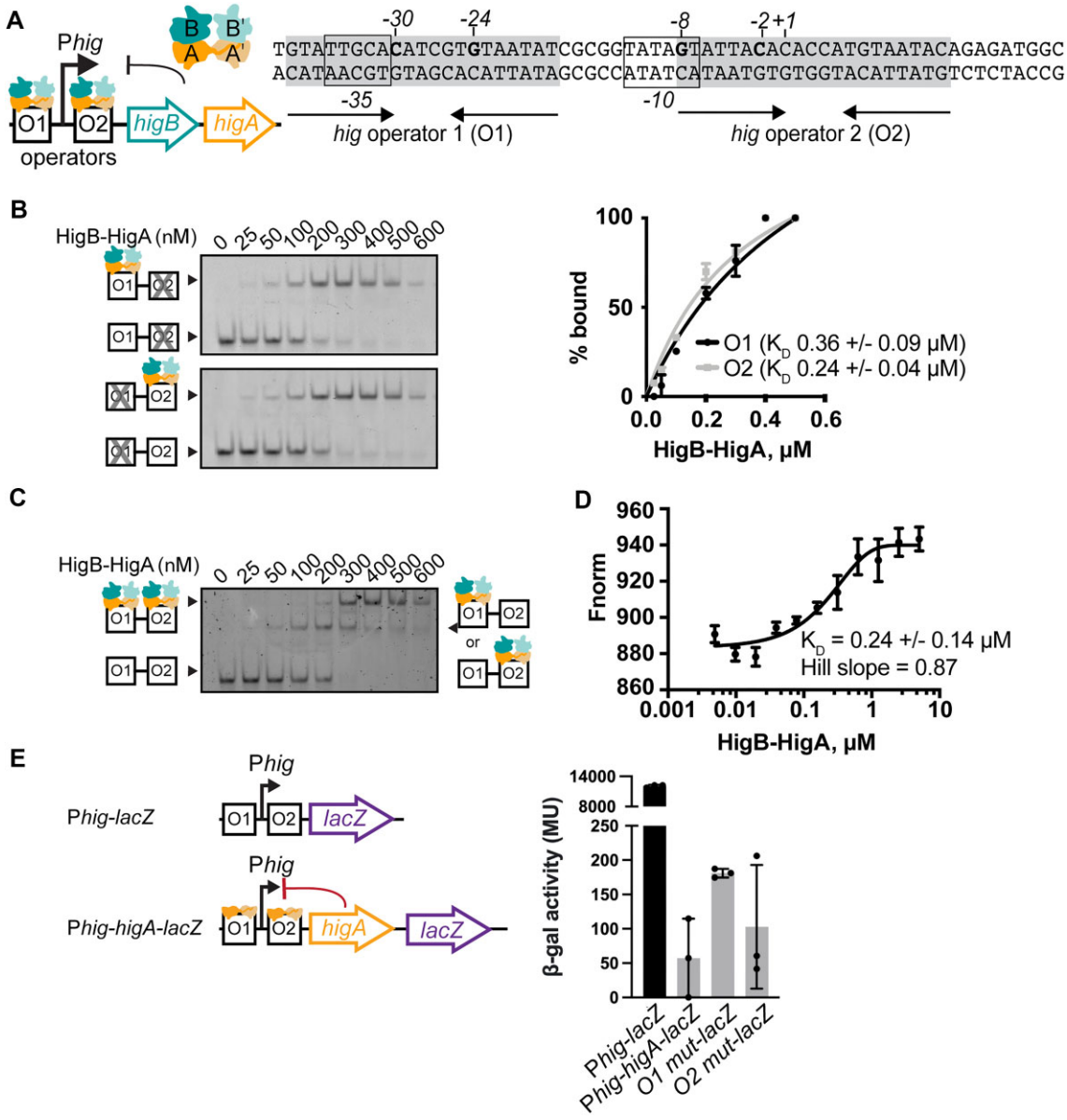

Figure 2. Binding of HigB–HigA to a single operator is sufficient for transcriptional repression at *hig*. (**A**) Organization of *hig* containing operators O1 and O2, P*hig*, *higB* toxin and *higA* antitoxin genes, the +1 transcriptional start site, and the −35 and −10 sites are indicated. The DNA sequence recognized by HigA is highlighted in gray and nucleotides that HigA directly contacts are shown in bold (C_{-30}, G_{-24}, G_{-8}, and C_{-2}). (**B**) EMSA of HigB–HigA binding to P*hig* containing only O1 (O2 scrambled; top), only O2 (O1 scrambled; bottom), and (**C**) both O1 and O2. Band intensities were plotted from EMSAs as the percent of HigB–HigA bound to DNA as a function of HigB–HigA concentration (concentrations used: 0–0.6 μM). The resulting plotted data represent the fit from which K_D values were calculated. (**D**) HigB–HigA binding assays measuring ligand-induced photo-enhancement of Cy5-labeled *hig* fluorescence. The DNA concentration was kept constant at 12.5 nM, while the concentration of HigB–HigA varied between 50 and 325 nM. Fluorescence values were baseline corrected and plotted against HigB–HigA concentration. Data of three independent measurements were fit with a specific binding with Hill slope equation ($n = 3$ independent measurements, error bars represent the SEM). (**E**) β-gal activity assays of *E. coli* BW25113 transformed with pQF50-P*hig-lacZ* (black bar) or pQF50-P*hig-higA-lacZ* (gray bar). Each operator site was tested using known operator mutations of either O1 ("O1 mut", $G_{-24}T$, $C_{-30}A$) or O2 ("O2 mut", $G_{-8}T$, $C_{-2}A$). In the case of pQF50-P*hig-higA-lacZ,* O1 mut, and O2 mut, β-gal activity was normalized against pQF50-P*hig-lacZ*.

an EMSA (Fig. 2B). The HigB–HigA complex was purified as previously described [26] and the *hig* O1 and O2 DNA consist of the entire 61-bp operator region (Supplementary Table S1). To determine whether HigB–HigA binds with high affinity to either O1 or O2, all 21 nucleotides in each operator were randomized individually (Supplementary Table S1). Each of these 21 nucleotides located in either O1 or O2 was previously shown to be protected upon HigA binding [61]. Therefore, any change in the mobility of the DNA band using a scrambled O1 or O2 would represent binding of HigB–HigA to either O1 or O2. The HigB–HigA complex binds to each of the two sites represented as a single molecular weight shift with similar dissociation binding constants (0.36 ± 0.09 μM for O1 and 0.24 ± 0.04 μM for O2) (Fig. 2B and Supplementary Table S2). This binding affinity is almost identical to what was seen when only the 21-bp O1 or O2 site was tested [47]. HigB–HigA was unable to bind to operator DNA containing both scrambled O1 and O2 DNA from *E. coli hig* indicating that the

P. vulgaris HigB–HigA•DNA repressor O1–O2 sites are distinct from the *E. coli* HigB–HigA-DNA repressor O1–O2 sites (Supplementary Fig. S1A and B). Titration of HigB–HigA with *hig* containing both O1 and O2 causes two distinct molecular weight shifts, indicating binding of HigB–HigA at each operator site (Fig. 2C). To determine a quantitative measure of HigB–HigA binding to both operators, we used a Cy5-labeled *hig* containing both O1 and O2 (61 bp). Increasing concentrations of HigB–HigA were added to *hig* that resulted in a dissociation binding constant of 0.24 ± 0.09 μM. The data were plotted to yield a Hill coefficient of 0.87, which indicates that the system is noncooperative (Fig. 2D).

To test transcriptional repression of wild-type HigB–HigA *in vivo*, we designed reporter constructs that encode *lacZ* in two different contexts: downstream of the *hig* promoter (P*hig-lacZ*) and downstream of *hig* but also containing *higA* (P*hig-higA-lacZ*) (Fig. 2E). The *hig-lacZ* construct reports on the activity of *hig* in the absence of the repressor HigA antitoxin, while the HigA-encoding pQF50-P*hig-higA-lacZ* construct reports on how HigA expression represses *hig*. P*hig-lacZ* shows robust β-gal activity, which is basal activity from *hig*. Expression of HigA efficiently represses *hig*, giving an ∼211-fold decrease in β-gal activity (Fig. 2E and Supplementary Fig. S2). To test whether HigA binding to a single operator region is sufficient for repression, we mutated either O1 or O2 recognition sequences important for HigA binding [47] and repeated the assays. Mutations to O1 only ($G_{-24}T/C_{-30}A$; "O1 mut") reduce β-gal activity by ∼67-fold, while mutations to O2 only ($G_{-8}T/C_{-2}A$; "O2 mut") reduce β-gal activity by ∼117-fold as compared to the wild-type P*hig* (Fig. 2E). These results show that HigA binding at both O1 and O2 results in optimal transcriptional repression and HigA binding at either O1 or O2 results in ∼3- and ∼2-fold decrease in repression.

Structure of $HigB_2$–$HigA_2$•*hig* O2 DNA

The HigB–HigA complex forms a tetrameric assembly with two HigB monomers and a HigA dimer (we will denote this as $HigB_2$–$HigA_2$) [26]. Each HigA antitoxin contains a fully functional HTH DNA-binding motif and forms an obligate $HigA_2$ dimer (Fig. 1). In the context of a $HigB_2$–$HigA_2$ complex, two HigA antitoxins—and thus two HTH motifs—bind to two inverted repeats of a single DNA operator (either O1 or O2) [26, 47]. To determine how HigB–HigA represses at its operator DNA, we determined a high-resolution X-ray crystal structure of HigB–HigA bound to the single O2 operator. We performed crystallization trials using two HigB–HigA constructs: a six-histidine (His_6) affinity tag located at the N terminus of HigB and a His_6 affinity tag located at the C terminus of HigA as previously described [40]. Both HigB–HigA constructs crystallized in the same crystallization condition; however, each structure resulted in a different ratio of HigB and HigA bound to O2. In the monoclinic space group crystal structure, the HigB–HigA-His_6•*hig* O2 complex was determined to 2.4 Å resolution by single-wavelength anomalous diffraction phasing and contained a $HigA_2$ dimer bound to two HigB monomers (Fig. 3). In this structure, residues 1–91 were built for each HigB monomer (92 total residues), all nucleotides [1–21] were built for the O2 DNA duplex, and residues 1–101 and 1–102 were built for HigA monomers (Supplementary Fig. S3).

In HigA's HTH motif, α2, loop 3, and α3 interact with the major groove of the operator O2 DNA (Fig. 3A). In the tetrameric $HigB_2$–$HigA_2$•*hig* O2 structure, HigA contacts the T_{-1}, G_{-2}, T_{-3}, and A_{-4} sequence on the *hig* negative strand [47] (Fig. 3A and B). HigA residue Arg40 interacts with the Hoogsteen face of G_{-2} to make the only sequence-specific protein–DNA contact. Residues Thr34 and Thr37 (from α3) contact the phosphate of G_{+7} while the sidechains of Ser23 (from loop 2), Ser39 (from α3), and Lys45 (from α3) are all within hydrogen bonding distance of nucleotides T_{-7}, A_{-6}, T_{-5}, and T_{-4}, respectively, which are located on the opposite DNA strand (Supplementary Fig. S4). Additionally, Ala36 and Thr34 form van der Waals interactions with the nucleobase C5 methyl of A_{-3}. These interactions are similar to those previously observed in the $HigA_2$•*hig* O2 DNA repressor complex [47] and are also present between HigA and O2 on the opposite strand, indicating that HigB binding to form the tetrameric $HigB_2$–$HigA_2$•*hig* O2 complex does not change interactions of $HigA_2$ with O2.

The termini of antitoxins are typically intrinsically disordered and this contributes to their proteolysis during environmental cues [21, 22, 34]. In the free $HigA_2$ structure [47], the N-terminus is also disordered (Supplementary Fig. S5A and B). Upon HigB binding, the HigA termini becomes ordered both in the free $HigB_2$–$HigA_2$ structure [26] and upon binding DNA ($HigB_2$–$HigA_2$•*hig* O2 DNA) (Fig. 3C and Supplementary Fig. S5C and D). The N- and C-termini of HigA form intramolecular interactions in addition to interactions with α1 of an adjacent HigB in the crystal lattice (Supplementary Fig. S5A and B). Specifically, N-terminal residues Arg2 (side chain) and Gln3 (backbone carbonyl) form salt bridges with C-terminal residues Glu80 and Arg77, respectively, and these interactions presumably stabilize the termini. Thus, binding of HigB stabilizes HigA both in the presence or absence and in the DNA.

To examine the transcriptional repression of wild-type HigB–HigA in response to excess HigB *in vivo*, we designed constructs that encode *lacZ* in two different contexts: downstream of the *hig* promoter (P*hig-lacZ*) and downstream of *hig* but also containing *higBhigA* (P*hig-higBhigA-lacZ*) (Fig. 4A). Cells were co-transformed with either of these constructs and with a construct that encodes HigB(H54A). The HigB(H54A) variant was used because this amino acid change renders the HigB toxin inactive and thereby prevents inhibition of growth [41, 49] (Supplementary Fig. S6). We also tested whether HigB(H54A) binds to HigA and we confirm that the mutation does not prevent the HigB–HigA interaction or expression (Supplementary Fig. S7). As expected, P*hig* alone shows robust β-gal activity (7000 MUs) because of the absence of transcriptional repressor HigA (Fig. 4A and Supplementary Fig. S8). When HigA is expressed (P*hig-higA-lacZ*), there is a reduction in β-gal activity, indicating HigA repression at P*hig* (1453 MUs) (Supplementary Fig. S8). HigB–HigA expression (P*hig-higBhigA-lacZ*) causes a reduction in β-gal activity indicating HigB–HigA repression at *hig* (867 MUs) is ∼1.6-fold weaker as compared to HigA alone. HigB–HigA expression also results in an ∼8-fold change of β-gal activity as compared to P*hig* alone. In an attempt to disrupt the molar ratio of HigB:HigA bound at the O1 and O2 repressor sites and to test the conditional cooperativity model, we overexpressed HigB(H54A), which resulted in a decrease in repression by ∼2.5-fold (Fig. 4A and Supplementary Fig. S8). These data suggest that while excess HigB may be able to disrupt the HigB–HigA complex, it cannot fully destabilize the complex to cause derepression at wild-type promoter-only levels *in vivo*.

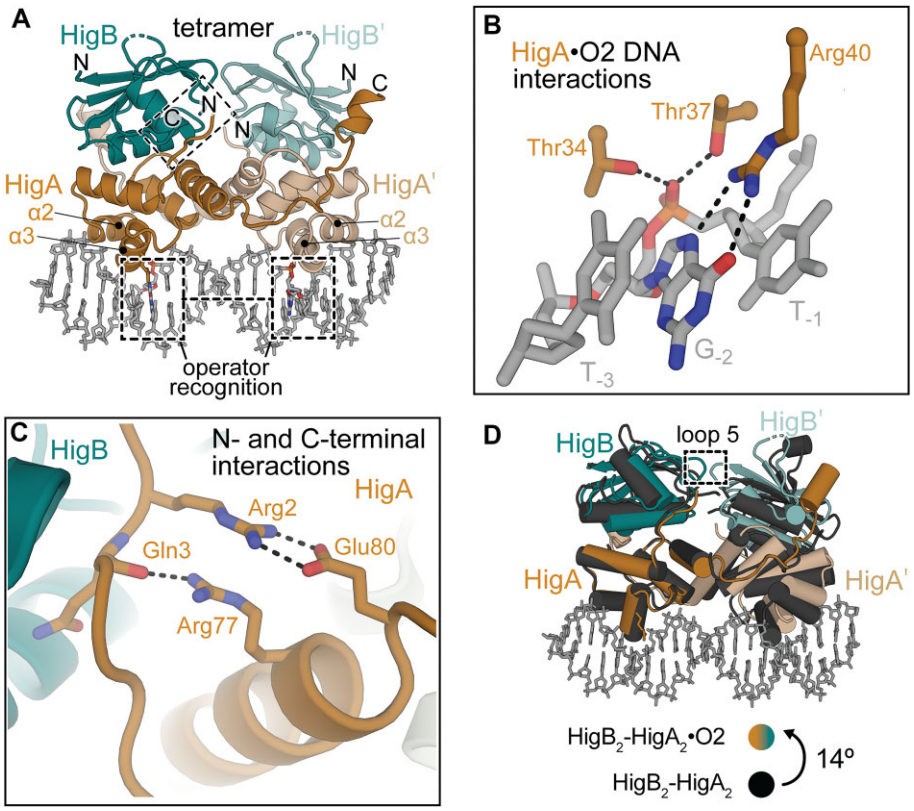

Figure 3. Structure of tetrameric $HigB_2$–$HigA_2$ bound to *hig* O2 DNA. (**A**) The 2.4-Å structure reveals that the O2 nucleotides T_{-1}, G_{-2},T_{-3}, and A_{-4} interacts with HigA via α2 and α3. The N- and C-terminal regions of HigA are boxed (PDB code 6W6U). (**B**) HigA Arg40 makes the only sequence specific interactions with the nucleobase of G_{-2}, while HigA residues Thr34 and Thr37 (both from α3) interact with the phosphate of G_{-2}. (**C**) The N- and C-terminal residues of HigA become ordered upon HigB binding. HigA residue Arg77 forms a hydrogen bond with the backbone carbonyl of Gln3 and Arg2, and Glu80 interacts via a salt bridge. (**D**) Comparison of the tetrameric $HigB_2$–$HigA_2$ complex (all black; PDB code 4MCX) and $HigB_2$–$HigA_2$•*hig* O2 DNA complex (PDB code 4MCX) reveals an ∼14° rotation of $HigB_2$–$HigA_2$ away from the O2 DNA.

To biochemically test whether HigB disrupts the HigB–HigA•*hig* O1–O2 DNA repressor complex, we performed EMSAs using purified HigB–HigA, HigB, and HigA (Fig. 4B). Addition of HigB alone to O1–O2 shows no change in mobility shift as expected, whereas addition of HigA reveals a slower moving band indicative of HigA binding to *hig* O1–O2 DNA. Addition of HigB–HigA reveals two additional higher molecular weight shifts when the same molar equivalent of HigB–HigA is added to *hig* O1-O2. The largest molecular weight band is smeary indicating possible multiple conformations of the HigB–HigA•*hig* O1–O2 DNA repressor complex. This smeariness goes away upon addition of 0.5 and 1.0 molar equivalents of HigB. Addition of >2 molar equivalents of HigB to HigB–HigA destabilizes the higher molecular weight band resulting in HigB–HigA disengaging from O1–O2 DNA (Fig. 4B).

Structure of HigB–$HigA_2$•*hig* O2 DNA

As noted above, both the tetrameric $HigB_2$–$HigA_2$•*hig* O2 DNA and trimeric HigB–$HigA_2$•*hig* O2 DNA crystal forms grew in the same crystallization condition and resulted in two different macromolecular structures (Supplementary Table S3). The His_6-HigB–$HigA_2$•*hig* O2 complex crystallized in the tetragonal space group $I4_1$, and the structure was determined by molecular replacement using the $HigA_2$ model (PDB code 6CF1) to a resolution of 2.8 Å. This structure contained a $HigA_2$ dimer bound to a single HigB (Fig. 5 and Supplementary Table S3). Residues 1–91 were built for each HigB monomer (92 total residues), residues 1–91 and 1–95 were built for each HigA (104 total residues), and all nucleotides [1–21] were built for the O2 DNA duplex (Supplementary Fig. S3). Interestingly, not all interactions seen in tetrameric $HigB_2$–$HigA_2$•*hig* O2 are conserved in the trimeric HigB–$HigA_2$•*hig* O2 structure. While critical interactions of HigA with the T_{-1}, G_{-2}, T_{-3}, and A_{-4} recognition sequence are maintained, α2 and α3 of the HTH DNA-binding motif slightly move away from the O2 DNA, no longer positioning Ser23 and Lys45 to hydrogen bond with the phosphates of T_{-7} and T_{-4} (Fig. 5B).

Comparison of the overall architecture of $HigB_2$–$HigA_2$•*hig* O2 to $HigB_2$–$HigA_2$ [26] or $HigA_2$ [47] reveals subtle changes that may be important for O2 DNA binding and transcriptional repression. Aligning analogous HigA monomers from the $HigB_2$–$HigA_2$•*hig* O2 and the $HigB_2$–$HigA_2$ structures (PDB code 4MCX) reveals an ∼14° displacement of the adjacent, second HigA promoter (Fig. 5D). Similarly, comparison of the free $HigA_2$ dimer (PDB code 6CF1) to $HigB_2$–$HigA_2$•*hig* O2 shows a rotation of HigA upon DNA binding, although the movement is not as large as compared to when HigB is present (∼8° rotations versus an ∼14° rotation) (Supplementary Fig. S9). Thus, $HigA_2$ reorients to bind DNA and HigB binding to a $HigA_2$•*hig* O2 complex minimally influences the protein–DNA interface.

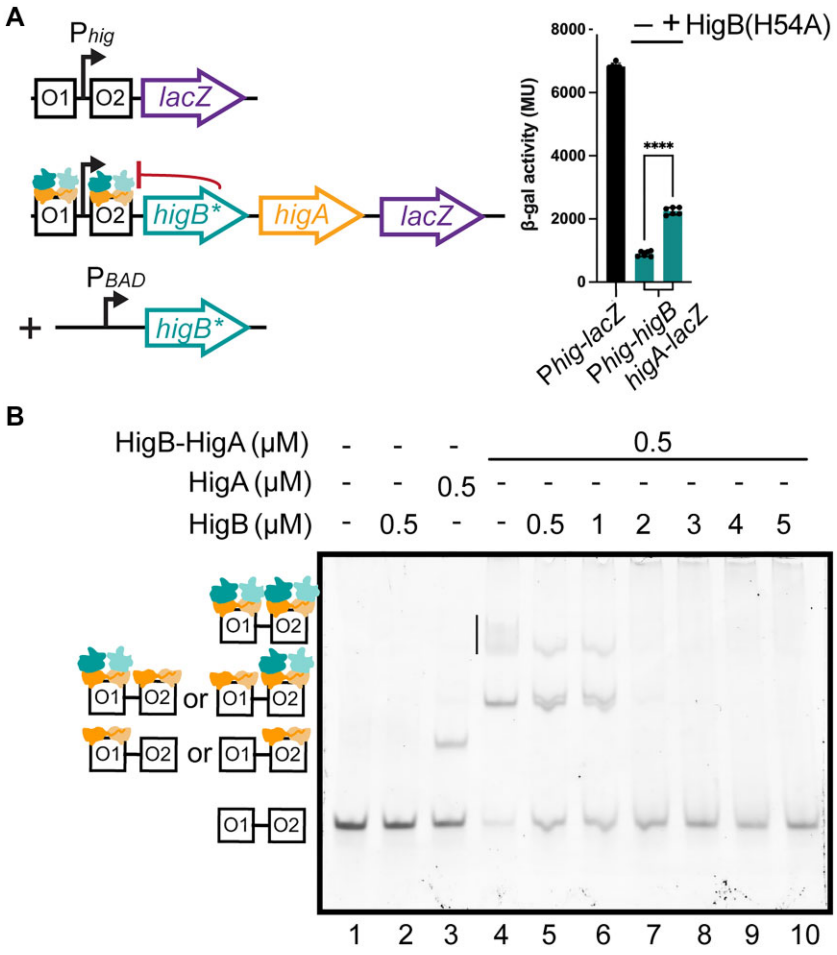

Figure 4. Formation of higher oligomeric states upon addition of HigB to the HigA•DNA complex is disrupted by excess HigB. (**A**) β-gal assays of *E. coli* BW25113 transformed with pOU254-P*hig-higB*(H54A)*higA-lacZ* or with also pBAD33-*higB*(H54A) (depicted in second and third rows of schematic). β-gal activity assays are shown as fold changes compared to *E. coli* BW25113 transformed alone with pOU254-P*hig* (top row of schematic). Error bars represent the mean ± SD of values of two independent experiments, each with three technical replicates. Asterisks represent the result of an unpaired *t*-test comparing the fold change in β-gal activity of *higBhigA* without HigB(H54A) to *higBhigA* with addition of HigB(H54A) (****P < .0001, $t = 13.79$, df = 10). (**B**) EMSA of HigB addition to the HigB–HigA•*hig* O1–O2 DNA complex. The *hig* O1–O2 DNA migrates the fastest (lane 1) and incubation with HigB alone does not cause a shift in the *hig* O1–O2 band (lane 2). Incubation with 0.5 μM HigA results in a slower movement of *hig* O1–O2 indicating HigA binding (lane 3). Addition of 0.5 μM HigB–HigA results in two slower moving but distinct *hig* O1–O2 bands where the slowest moving band is smeary (vertical line; lane 4). Equivalent molar amounts of HigB (lanes 5 and 6) result in two similar higher molecular weight complexes as HigB–HigA alone but the slowest moving band lacks the smeariness and the band is more defined. When HigB exceeds the molar excess of HigB–HigA, the two molecular weight shifts are no longer observed indicating that neither HigA nor HigB binds (lanes 7–10).

Global comparison of the $HigB_2$–$HigA_2$•*hig* O2 structure with the HigB–$HigA_2$•*hig* O2 structure reveals only an ∼1° difference emphasizing how similar the two structures are (Fig. 5D). Likewise, there are very little differences in the position of $HigA_2$ bound to O2 [47] in the absence or presence of HigB. Thus, it does not appear that HigB binding influences the position of $HigA_2$ on DNA. The largest structural change results from either $HigA_2$ or $HigB_2HigA_2$ binding to DNA (∼14° rotation; Fig. 3D). In the context of the $HigB_2$–$HigA_2$•*hig* O2 structure, the HigA N- and C-terminal residues move from a disordered to ordered transition where Arg2 and Gln3 interact with Arg77 and Glu80 (Fig. 3C). We find that even a single HigB binding in the trimeric HigB–$HigA_2$•*hig* O2 structure causes these terminal residues to become ordered (Fig. 5C).

A curious crystallization note for the trimeric HigB–$HigA_2$•*hig* O2 complex is that there is an adjacent molecule in the neighboring asymmetric unit that overlaps with the missing HigB (Supplementary Fig. S10). This ejection of HigB from the HigB–HigA complex is surprising given the known tight interactions of toxins and antitoxins for each other where affinities are typically sub-nanomolar [24, 62–64]. Therefore, we think it is unlikely that the trimeric HigB–$HigA_2$•*hig* O2 complex resulted from crystal packing. Interestingly, the structures of both HigB–HigA complexes with the different placement of the His_6 tag were solved and both were found to be tetrameric $HigB_2$–$HigA_2$ in the absence of DNA [26]. Taken together, we propose that there is likely a mixture of both trimeric and tetrameric HigB–HigA complexes bound to DNA repressor sites consistent with mixed ratios of TA from other systems [23, 30, 65].

Trimeric HigB–$HigA_2$ represses P*hig* to a greater extent than $HigB_2$–$HigA_2$

At this point, we assume that the majority of the HigB–HigA complex used in the EMSA is tetrameric $HigB_2$–$HigA_2$ because prior $HigB_2$–$HigA_2$ structures show that the com-

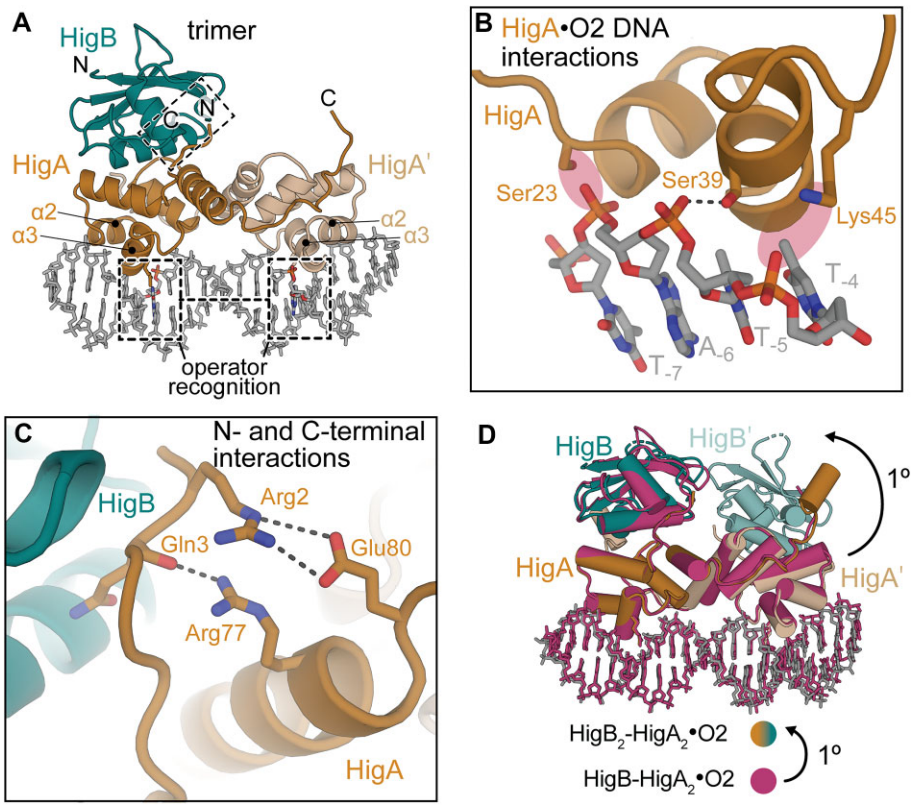

Figure 5. Structure of trimeric HigB–$HigA_2$ bound to *hig* O2 DNA. (**A**) The 2.8-Å structure of trimeric HigB–$HigA_2$•*hig* O2 DNA (PDB code 6WFP). HigA recognizes the T_{+6}, G_{+7}, T_{+8}, and A_{+9} DNA region via α2 and α3. N- and C-terminal regions of HigA are boxed. (**B**) In the $HigB_2$–$HigA_2$•*hig*O2 DNA structure (PDB code 6W6U), HigA residues Ser23, Ser39, and Lys45 interact with the backbone phosphate of T_{-7}, T_{-5}, and T_{-4}, respectively, to rigidify the T_{-1}, G_{-2}, T_{-3}, and A_{-4} sequence for nucleotide-specific recognition on the opposite strand. In the trimeric HigB–$HigA_2$•*hig* O2 structure, only Ser39 interacts with the phosphate backbone and Ser23 and Lys45 are too distant (red highlighted region). (**C**) The N- and C-terminal residues of HigA become ordered upon a single HigB monomer binding similar to when two HigB monomers bind. (**D**) Comparison of trimeric HigB–$HigA_2$•*hig* O2 DNA (PDB code 6WFP) and tetrameric $HigB_2$–$HigA_2$•*hig*O2 DNA (PDB code 6W6U) reveals incredibly similar structures with an RMSD of 0.7 Å (for 1479 equivalent atoms) and less than an ∼1° rotation.

plex is tetrameric [26]. To test whether a trimeric HigB–$HigA_2$ complex represses transcription to the same extent as tetrameric $HigB_2$–$HigA_2$, we attempted to engineer such a trimeric variant. Comparison of the $HigB_2$–$HigA_2$ structure with the $HigB_2$–$HigA_2$•*hig* O2 DNA structure shows that the two HigB monomers are closer to each other in the presence of DNA (Fig. 6A). In particular, HigB loop 5 (L5) located at the interface of the HigB monomers moves ∼4 Å towards each other (Fig. 6A). Additionally, PISA analysis of the HigB–HigA structure (PDB code 4MCX) also reveals an interface between HigB monomers of 228.8 $Å^2$ mainly at loop L5. We therefore decided to extend loop L5 by the addition of a short, flexible sequence of four residues (Asn, Gly, Asn, Gly; we denote this as HigB(L5ext)–$HigA_2$). This extension is predicted to prevent concurrent binding of two HigB monomers to $HigA_2$•*hig* O2 repressor complex (Fig. 6A). Expression and purification of HigB(L5ext)–$HigA_2$ showed a delayed elution of the complex from the size exclusion column as compared to wild-type $HigB_2$–$HigA_2$, at a volume corresponding to a molecular weight of ∼42 kDa (compared to 56 kDa for wild-type $HigB_2$–$HigA_2$; Fig. 6B). The difference in apparent molecular weights indicates that the HigB(L5ext)–$HigA_2$ complex is ∼14 kDa smaller than the wild-type complex that roughly corresponds to a HigB monomer (molecular weight of ∼13 kDa). To assess its thermal stability, we performed nano-differential scanning fluorimetry (nano-DSF) that provides information on the melting temperature (T_m) of the complex. Since this measurement is not at equilibrium, the inflection point is known as T_i. HigB(L5ext)–$HigA_2$ is ∼5°C less thermostable than wild-type $HigB_2$–$HigA_2$ (60.5°C versus 54.0°C) consistent with an altered oligomeric state (Fig. 6C).

One possibility that we wanted to explore was whether *hig* is responsive to changing HigB toxin levels *in vivo* in the presence of a trimeric HigB–$HigA_2$•*hig* O2 DNA repressor considering that toxin overexpression in the Phd–Doc, CcdB–CcdA, and RelB–RelE TAs and now HigB–HigA can relieve repression [21, 22, 34] (Fig. 4). For this assay, we overexpressed the same inactive HigB(H54A) variant used previously with tetrameric $HigB_2$–$HigA_2$. Engineered HigB(L5ext)–$HigA_2$ robustly represses transcription ∼26-fold more than what we presume is tetrameric $HigB_2$–$HigA_2$ (897 MUs versus 34 MUs; compare Figs 6D and 4A; Supplementary Fig. S8). Excess HigB(H54A) has little to no effect on repression when trimeric HigB–$HigA_2$ is bound at *hig* (34 MUs versus 36 MUs; Fig. 6D and Supplementary Fig. S8), likely because the engineered loop L5 prevents another HigB from binding. These results show differences in *hig* repression and derepression that are dependent on whether a trimeric HigB–$HigA_2$ or a tetrameric $HigB_2$–$HigA_2$ binds at *hig* repressor sites that, in turn, change its responsiveness to excess HigB toxin.

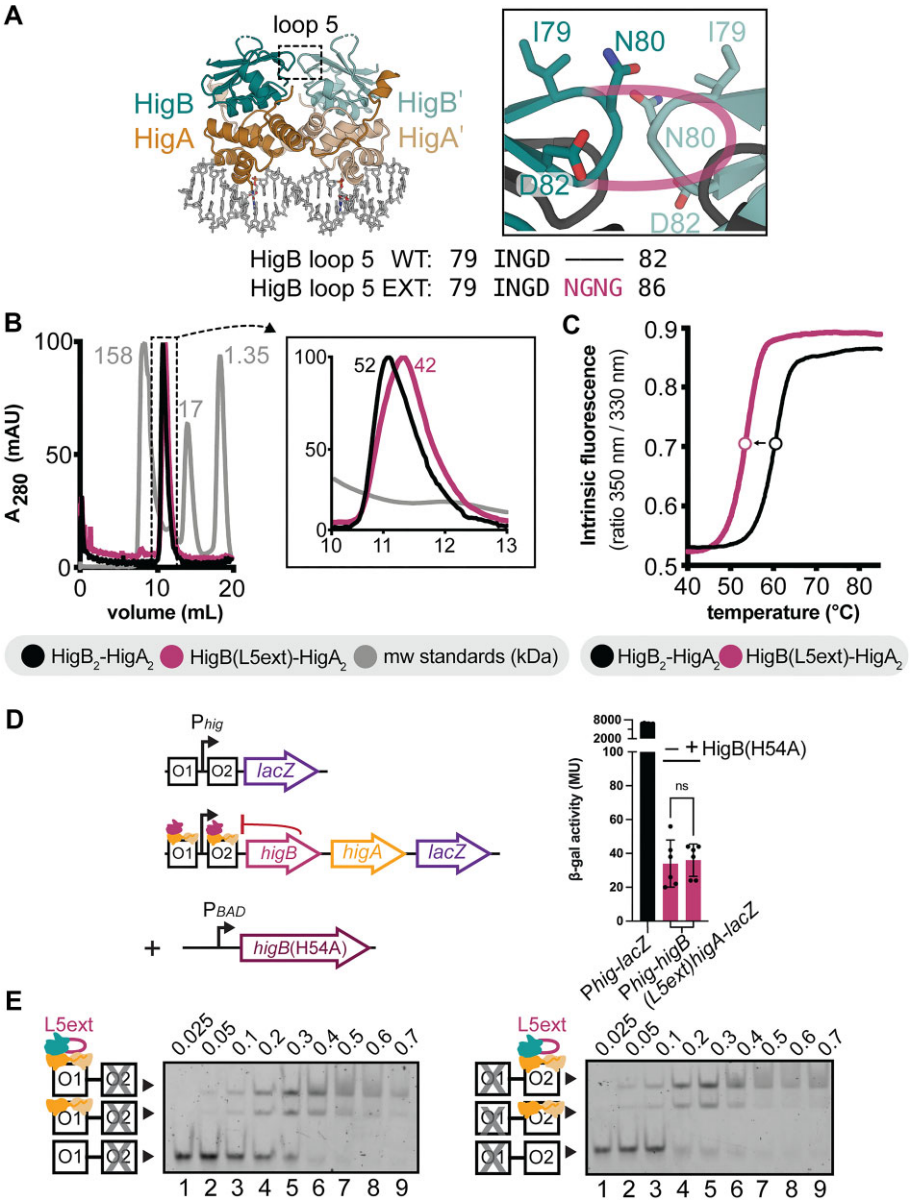

Figure 6. Engineering a trimeric HigB–$HigA_2$ complex. (**A**) To prevent two HigB monomers binding, loop L5 of HigB was extended by the insertion of four residues (Asn, Gly, Asn, Gly (NGNG); "L5ext,") after residue Asp82. A zoomed in view of this interaction is shown in the dotted box (right). The theoretical extension of loop L5 is shown in magenta with the wild-type HigB and HigB(L5ext) amino acid alignment shown beneath. (**B**) Size exclusion chromatography (SEC) of purified wild-type $HigB_2$–$HigA_2$ shows an elution volume that corresponds to a molecular weight of 52 kDa. HigB(L5ext)–$HigA_2$ complex elutes at a volume corresponding to a molecular weight of 42 kDa with the inset showing a zoomed in view. Molecular weight standards are shown in gray. (**C**) Nano-DSF analysis of wild-type $HigB_2$–$HigA_2$ and HigB(L5ext)–$HigA_2$ shows that the HigB(L5ext)–$HigA_2$ complex has ∼5°C lower T_i value than $HigB_2$–$HigA_2$. Fluorescence values were normalized to the highest tested temperature and the boundary of each line represents the mean ± SD of values from three independent experiments. (**D**) β-gal activity assays of *E. coli* BW25113 transformed with pOU254-P*hig*-*higB*(H54A, L5ext)-*higA*-*lacZ* or with pBAD33-*higB*(H54A*)* (left schematic). Fold change in β-gal activity is compared to *E. coli* BW25113 transformed with pOU254-P*hig* (top left row of schematic). Error bars represent the mean ± SD of values of two independent experiments, each with three technical replicates. N.S. represents the non-significance result of an unpaired *t*-test comparing the fold change in β-gal activity of the *higB*(L5ext)–*higA* without HigB(H54A) to *higB*(L5ext)–*higA* with addition of HigB(H54A) (P = .5807, $t = 0.5708$, df = 10, n.s.). (**E**) EMSA of HigB(L5ext)–$HigA_2$ binding to *hig* O1 DNA (O2 scrambled; left) or to O2 DNA (O1 scrambled; right).

We next attempted to determine whether the binding of engineered HigB(L5ext)–$HigA_2$ to *hig* O1 or O2 retained the noncooperative features we observed when $HigB_2$–$HigA_2$ binds *hig* O1 or O2 (Fig. 2B). The HigB(L5ext)–$HigA_2$ complex was purified and the same *hig* O1 and O2 DNA was used as in prior EMSAs (Fig. 2A and B). Titration of HigB(L5ext)–$HigA_2$ with *hig* containing either O1 or O2 (with each of the other scrambled to allow for only one available *hig* operator) unexpectedly causes two distinct molecular weight shifts (Fig. 6E). While the HigB(L5ext)–$HigA_2$ complex elutes as one defined SEC peak suggestive of the complex adopting one defined oligomeric state, in the presence of either *hig* O1 or O2, two molecular weight shifts occur indicating two distinct binding events. Since $HigA_2$ is an obligate dimer [47], we hypothesize that binding to either *hig* O1 or O2 changes the molecular interactions and thus affinities be-

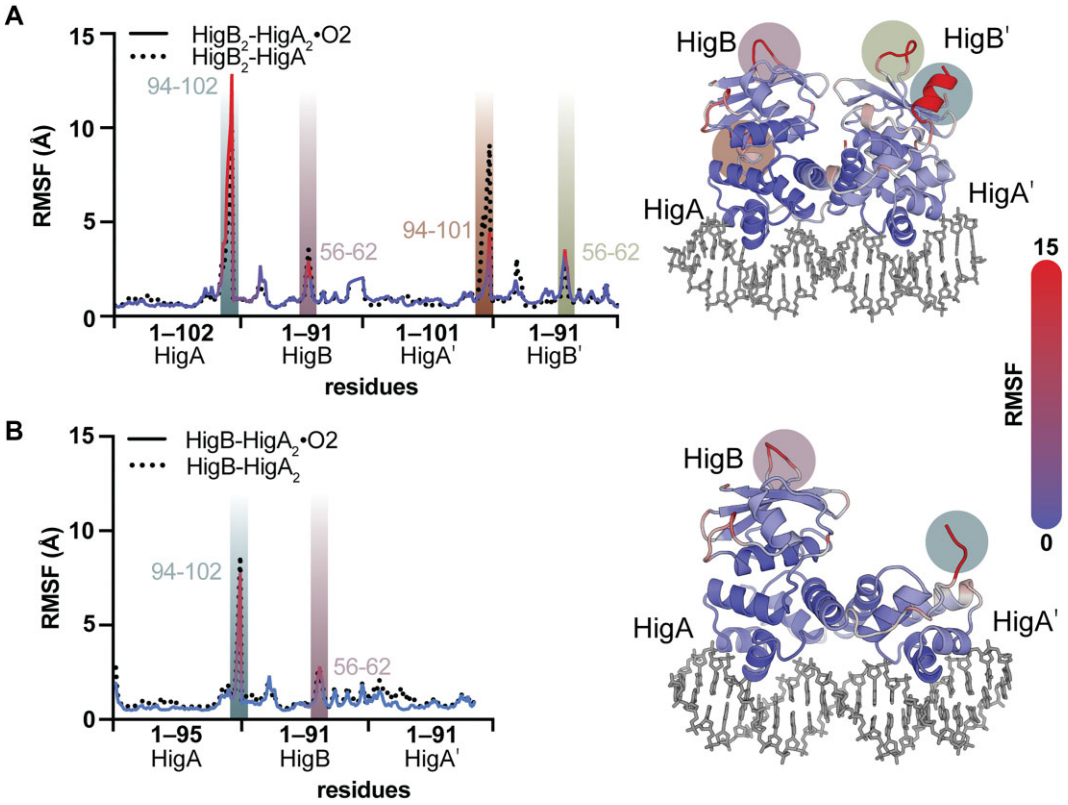

Figure 7. Trimeric HigB–$HigA_2$ and tetrameric $HigB_2$–$HigA_2$ exhibit similar dynamics in the presence or absence of *hig* O2 DNA. RMSFs of Cα atoms for each residue in the (**A**) HigB–$HigA_2$ or (**B**) $HigB_2$–$HigA_2$ complexes are calculated from 1-ms MD trajectories. Regions that have increased RMSFs are indicated with highlighted bars that correspond to their positions on the HigB–HigA•*hig* O2 structures (right). High RMSF spikes correlate to either labile C-termini of HigA or HigB loop regions with colored circles corresponding to the highlighted bars on the left.

tween HigB(L5ext) with the $HigA_2$ dimer. This change allows for the $HigA_2$ dimer to bind independently to either *hig* O1 or O2 but permits HigB(L5ext) binding to the $HigA_2$–DNA repressor complex.

$HigB_2$–$HigA_2$•*hig* O2 and HigB–$HigA_2$•*hig* O2 complexes exhibit similar dynamics

The structure of the trimeric HigB–$HigA_2$•*hig* O2 complex is intriguing as most models that describe the transcriptional regulation of type II TA systems conclude that such a toxin:antitoxin ratio is more stable than the fully loaded complex [22, 29, 64]. However, prior to our new structure, there has been no biochemical or direct evidence for the existence of this oligomeric state. To assess the dynamics of both complexes in the presence or absence of O2, we performed MD simulations of four complexes: $HigB_2$–$HigA_2$ and HigB–$HigA_2$ in the presence or absence of O2 (Fig. 7). The trimeric HigB–$HigA_2$ complex in the absence of DNA has not been solved and we generated the model based upon the HigB–$HigA_2$•*hig* O2 structure. We obtained 1-μs-long MD trajectories of each complex and subsequently performed RMSF analysis. This analysis reveals overall comparable dynamics: in tetrameric $HigB_2$–$HigA_2$, binding to O2 only marginally affects dynamics, with the largest effects observed at intrinsically flexible regions such as the C termini of the HigA monomers (residues 94–102) and loop 3 of HigB (residues 56–62) (Fig. 7A). In trimeric HigB–$HigA_2$, similar trends are observed, confirming that both oligomeric states represent similarly stable, DNA-bound complexes (Fig. 7B). One noted difference is that in the trimeric HigB–$HigA_2$•*hig* O2 complex, the C-terminus of one of the two HigAs is disordered and is not modeled. The binding of two HigB monomers causes the C-terminus of HigA to regain order, but while the C-terminus of both HigA monomers can be modeled, this region still exhibits dynamic behavior.

Discussion

In this study, we focus on the regulation of the HigB–HigA TA module first identified on the antibiotic resistant Rts1 plasmid associated with a urinary tract infection caused by *P. vulgaris* [38]. Our prior work revealed that while the *P. vulgaris* HigB toxin adopts a canonical microbial ribonuclease fold that is similar to other members of the RelE family [26], the structure of the HigA antitoxin and its transcriptional repression at the *hig* O2 site suggested that its regulation was different from other known type II modules. For example, HigA does not wrap around the HigB toxin to suppress toxicity and the binding of the HigB–HigA complex to *hig* O2 DNA is weaker, rather than stronger, than HigA alone [49]. Based upon these differences, we therefore sought to understand how the diverse architecture of HigB–HigA influences transcriptional repression at *hig* operator sites.

Other type II TA modules including CcdB–CcdA, Kis–Kid, RelB–RelE, Phd–Doc, and TacT–TacA are regulated by changing toxin levels that alter TA formation at DNA operator sites and thus the repression/derepression cycle [21–23, 30, 66].

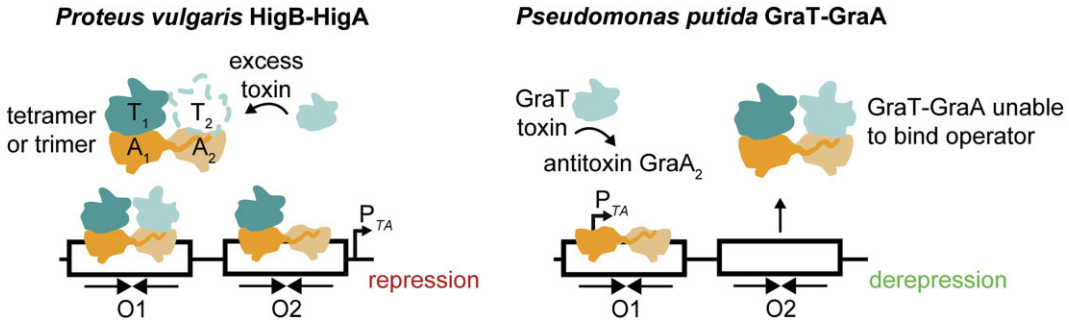

Figure 8. Diverse modes of transcriptional repression within the HigB–HigA family. Toxin (T) and antitoxin (A) proteins form multimeric complexes that bind operator sites (O1 and O2) that overlap with their promoters (P_{TA}) to repress transcription. In the *P. vulgaris* HigB–HigA system (left), diverse oligomeric complexes of HigB–HigA sufficiently repress transcription. In contrast, the GraT toxin of the GraT–GraA TA system acts as a derepressor for the *gra* operon by binding to the GraA antitoxin relieving repression. GraT–GraA and HigB–HigA complexes have high sequence identity and structural homology indicating that even among evolutionarily conserved HigB–HigA family members, the modes of transcriptional repression vary significantly.

In the TacT–TacA system, the two TacA antitoxins contact a single TacT toxin for suppression and its changing oligomeric state contributes to its repression–derepression cycle, indicating that this TA is regulated in a unique way. [65]. In the RelB–RelE TA system where the RelE toxin is very similar to HigB, the trimeric $RelB_2$–RelE is proposed to bind with high affinity to the *relO* operator, while the tetrameric $RelB_2$–$RelE_2$ represents a low-affinity complex for *relO* that causes derepression [22, 29]. However, the tetrameric $RelB_2$–$RelE_2$ is the only oligomeric complex observed [29]. The conditional cooperativity model for RelB–RelE regulation is attractive because it permits the system to be responsive to changing levels of toxin. However, at this point, there are limited biochemical and structural data that show examples of these changing oligomeric states.

The structure of apo *P. vulgaris* HigB–HigA reveals a tetrameric architecture with two HigB and two HigA protomers ($HigB_2$–$HigA_2$) [26]. The HigB toxin does not increase the affinity of HigA for the *hig* operator, and thus, *hig* does not appear to be regulated by conditional cooperativity. In fact, HigA binds to *hig* O2 two-fold tighter than HigB–HigA in contrast to the important role of RelE in optimally suppressing *relO* by increasing the affinity of RelB [22]. Since we saw neither cooperative binding of HigB–HigA binding at *hig* O1–O2, we concluded that the HigB–HigA system was not regulated by conditional cooperativity. Therefore, it was surprising when we serendipitously solved two different structures of the HigB–HigA•*hig* O2 complex that differ in their molar ratios of HigA antitoxin to the HigB toxin. The different oligomeric HigB–HigA complexes bound to *hig* O2 thus capture how different ratios of toxin:antitoxin complexes interact with a single operator. The trimeric HigB–$HigA_2$•*hig* O2 DNA structure was especially unexpected given that the apo tetrameric $HigB_2$–$HigA_2$ form predominates as observed in prior structural studies [26]. In an attempt to perturb the system *in vivo* by increasing HigB concentrations in the presence of what we presume is predominantly the tetrameric $HigB_2$–$HigA_2$ complex bound at *hig* O1–O2 operators, we find an ∼2.5-fold increase in transcriptional derepression (Fig. 4A and Supplementary Fig. S8). These data show that while HigB does not function as a transcriptional co-repressor at *hig*, HigB toxin can disrupt interactions between HigB–HigA and *hig* and thus is a transcriptional derepressor. Engineering a trimeric HigB(L5ext)–$HigA_2$ complex revealed a ∼26-fold increase in transcriptional repression over the tetrameric $HigB_2$–$HigA_2$ indicating either a tighter binding or avidity of the trimer complex for *hig*. Excess HigB toxin has little to no effect on derepression of the trimeric HigB(L5ext)–$HigA_2$, suggesting that this engineered complex likely prevents binding of a second HigB because of the loop L5 extension. Molecular dynamic simulations of both the trimeric and tetrameric HigB–HigA•*hig* O2 repressor complexes show that each complex has similar dynamics and stability when bound to DNA, offering further support for the ability of both oligomeric states to contribute to repression. Together, these results point to a system where the toxin is not a co-repressor yet is a derepressor, an example of an atypical HigB–HigA system.

HigB–HigA shares high sequence (29%) and structural similarity with the GraT–GraA system from *P. putida* [36] (Fig. 8; overall RSMD of 2.5 Å for residues 23–92). Despite these structural similarities, there are several key differences in regulation. Although the GraT toxin adopts a microbial ribonuclease fold similar to HigB, the N-terminal 23 amino acids remain disordered in complex with antitoxin GraA, while in the HigB structure, the N-terminal HigB residues form interactions with a HigA monomer. Another significant distinction is that GraA binding to its operator causes high levels of repression and the GraT toxin is unable to bind to GraA while GraA is simultaneously bound to DNA. While both GraT and HigB toxins are not co-repressors in contrast to other type II toxins, in fact, the way these two structurally similar toxins function is completely different. The GraT toxin dissociates GraA antitoxin from its operator causing derepression, while HigB can bind to HigA-*hig* O2 complex. Additionally, the binding of multiple GraA antitoxins at its operator is highly cooperative, while there appears to be no cooperative binding of the HigA antitoxin to *hig* [47] (Fig. 2). These functional differences between the GraT–GraA and HigB–HigA systems are surprising given their high structural homology.

The results presented here provide new insights into the transcriptional regulation of plasmid-associated *higB-higA* and add to the growing diversity of mechanisms used to balance transcriptional responses of these abundant bacterial gene pairs. In the future, additional biophysical studies are needed to reconcile the role of changing macromolecular complex formation in the regulation of TA pairs and to align these properties with transcriptional responsiveness.

Acknowledgements

We thank F.M. Murphy IV and staff members of the NE-CAT beamlines for assistance during data collection and G.L. Conn and other Dunham lab members for critical reading of the manuscript. Additional data were collected at the Southeast Regional Collaborative Access Team (SER-CAT) 22-ID (or 22-BM) beamline at the Advanced Photon Source, Argonne National Laboratory. SER-CAT is supported by its member institutions (www.ser-cat.org/members.html) and equipment grants (S10RR25528 and S10RR028976) from the National Institutes of Health. Use of the Advanced Photon Source was supported by the U.S. Department of Energy, Office of Science, Office of Basic Energy Sciences, under Contract No. DE-AC02-06CH11357.

Author contributions: Ian J. Pavelich (Conceptualization [equal], Data curation [equal], Formal analysis [equal], Investigation [equal], Writing—original draft [equal], Writing—review & editing [equal]), Marc A. Schureck (Conceptualization [equal], Data curation [equal], Formal analysis [equal], Investigation [equal], Writing—original draft [equal], Writing—review & editing [equal]), Pooja Srinivas (Formal analysis [supporting], Investigation [supporting], Writing—original draft [supporting], Writing—review & editing [supporting]), Taylor M. Blackburn (Formal analysis [supporting], Investigation [supporting], Writing—review & editing [supporting]), Dongxue Wang (Investigation [supporting]), Eric D. Hoffer (Investigation [supporting], Writing—original draft [supporting]), Michelle Boamah (Investigation [supporting]), and Kimberly Zaldana (Investigation [supporting]).

Supplementary data

Supplementary data is available at NAR online.

Conflict of interest

None declared.

Funding

Research reported in this publication was partially supported by National Institutes of Health R01GM093278 (C.M.D.), NIH R35 GM156629 (C.M.D.), NIH 5T32 GM8367 (M.A.S.), NIH NRSA F31 Fellowship GM108351 (M.A.S.), NIH T32 AI106699 (T.M.B.) and a Burroughs Wellcome Fund Investigator in the Pathogenesis of Infectious Disease award (C.M.D.). This work is based upon research conducted at the Northeastern Collaborative Access Team beamlines, which are funded by the National Institute of General Medical Sciences from the National Institutes of Health (P30 GM124165). The Eiger 16M detector on 24-ID-E is funded by a NIH-ORIP HEI grant (S10OD021527). This research used resources of the Advanced Photon Source, a U.S. Department of Energy (DOE) Office of Science User Facility operated for the DOE Office of Science by Argonne National Laboratory under Contract No. DE-AC02-06CH11357. Funding to pay the Open Access publication charges for this article was provided by National Institutes of Health.

Data availability

Crystallography, atomic coordinates, and structure factors have been deposited in the Protein Data Bank, www.pdb.org (PDB codes 9CHL and 9CHN).

References

1. Gerdes K, Rasmussen PB, Molin S. Unique type of plasmid maintenance function: postsegregational killing of plasmid-free cells. *Proc Natl Acad Sci USA* 1986;**83**:3116–20. https://doi.org/10.1073/pnas.83.10.3116
2. Karoui H, Bex F, Dreze P *et al.* Ham22, a mini-F mutation which is lethal to host cell and promotes recA-dependent induction of lambdoid prophage. *EMBO J* 1983;**2**:1863–8. https://doi.org/10.1002/j.1460-2075.1983.tb01672.x
3. Ogura T, Hiraga S. Mini-F plasmid genes that couple host cell division to plasmid proliferation. *Proc Natl Acad Sci USA* 1983;**80**:4784–8. https://doi.org/10.1073/pnas.80.15.4784
4. Bravo A, de Torrontegui G, Diaz R. Identification of components of a new stability system of plasmid R1, ParD, that is close to the origin of replication of this plasmid. *Mol Gen Genet* 1987;**210**:101–10. https://doi.org/10.1007/BF00337764
5. Tsuchimoto S, Ohtsubo H, Ohtsubo E. Two genes, pemK and pemI, responsible for stable maintenance of resistance plasmid R100. *J Bacteriol* 1988;**170**:1461–6. https://doi.org/10.1128/jb.170.4.1461-1466.1988
6. Lehnherr H, Maguin E, Jafri S *et al.* Plasmid addiction genes of bacteriophage P1: doc, which causes cell death on curing of prophage, and phd, which prevents host death when prophage is retained. *J Mol Biol* 1993;**233**:414–28. https://doi.org/10.1006/jmbi.1993.1521
7. Pandey DP, Gerdes K. Toxin–antitoxin loci are highly abundant in free-living but lost from host-associated prokaryotes. *Nucleic Acids Res* 2005;**33**:966–76. https://doi.org/10.1093/nar/gki201
8. Makarova KS, Wolf YI, Koonin EV. Comprehensive comparative-genomic analysis of type 2 toxin–antitoxin systems and related mobile stress response systems in prokaryotes. *Biol Direct* 2009;**4**:19. https://doi.org/10.1186/1745-6150-4-19
9. Leplae R, Geeraerts D, Hallez R *et al.* Diversity of bacterial type II toxin–antitoxin systems: a comprehensive search and functional analysis of novel families. *Nucleic Acids Res* 2011;**39**:5513–25. https://doi.org/10.1093/nar/gkr131
10. Guan J, Chen Y, Goh YX *et al.* TADB 3.0: an updated database of bacterial toxin–antitoxin loci and associated mobile genetic elements. *Nucleic Acids Res* 2024;**52**:D784–90. https://doi.org/10.1093/nar/gkad962
11. Fraikin N, Goormaghtigh F, Van Melderen L. Type II toxin–antitoxin systems: evolution and revolutions. *J Bacteriol* 2020;**202**:e00763-19. https://doi.org/10.1128/JB.00763-19
12. Makarova KS, Wolf YI, Koonin EV. The basic building blocks and evolution of CRISPR–CAS systems. *Biochem Soc Trans* 2013;**41**:1392–400. https://doi.org/10.1042/BST20130038
13. Harms A, Maisonneuve E, Gerdes K. Mechanisms of bacterial persistence during stress and antibiotic exposure. *Science* 2016;**354**:aaf4268. https://doi.org/10.1126/science.aaf4268
14. LeRoux M, Laub MT. Toxin–antitoxin systems as phage defense elements. *Annu Rev Microbiol* 2022;**76**:21–43. https://doi.org/10.1146/annurev-micro-020722-013730
15. Page R, Peti W. Toxin–antitoxin systems in bacterial growth arrest and persistence. *Nat Chem Biol* 2016;**12**:208–14. https://doi.org/10.1038/nchembio.2044
16. Harms A, Brodersen DE, Mitarai N *et al.* Toxins, targets, and triggers: an overview of toxin–antitoxin biology. *Mol Cell* 2018;**70**:768–84. https://doi.org/10.1016/j.molcel.2018.01.003
17. Jurenas D, Fraikin N, Goormaghtigh F *et al.* Biology and evolution of bacterial toxin–antitoxin systems. *Nat Rev Microbiol* 2022;**20**:335–50. https://doi.org/10.1038/s41579-021-00661-1

18. Loris R, Garcia-Pino A. Disorder- and dynamics-based regulatory mechanisms in toxin–antitoxin modules. *Chem Rev* 2014;**114**:6933–47. https://doi.org/10.1021/cr400656f
19. Gotfredsen M, Gerdes K. The *Escherichia coli* relBE genes belong to a new toxin–antitoxin gene family. *Mol Microbiol* 1998;**29**:1065–76. https://doi.org/10.1046/j.1365-2958.1998.00993.x
20. Magnuson R, Yarmolinsky MB. Corepression of the P1 addiction operon by Phd and Doc. *J Bacteriol* 1998;**180**:6342–51. https://doi.org/10.1128/JB.180.23.6342-6351.1998
21. Afif H, Allali N, Couturier M *et al.* The ratio between CcdA and CcdB modulates the transcriptional repression of the ccd poison–antidote system. *Mol Microbiol* 2001;**41**:73–82. https://doi.org/10.1046/j.1365-2958.2001.02492.x
22. Overgaard M, Borch J, Jorgensen MG *et al.* Messenger RNA interferase RelE controls relBE transcription by conditional cooperativity. *Mol Microbiol* 2008;**69**:841–57. https://doi.org/10.1111/j.1365-2958.2008.06313.x
23. Grabe GJ, Giorgio RT, Wieczor M *et al.* Molecular stripping underpins derepression of a toxin–antitoxin system. *Nat Struct Mol Biol* 2024;**31**:1050–60. https://doi.org/10.1038/s41594-024-01253-2
24. Brown BL, Lord DM, Grigoriu S *et al.* The *Escherichia coli* toxin MqsR destabilizes the transcriptional repression complex formed between the antitoxin MqsA and the mqsRA operon promoter. *J Biol Chem* 2013;**288**:1286–94. https://doi.org/10.1074/jbc.M112.421008
25. Ruangprasert A, Maehigashi T, Miles SJ *et al.* Mechanisms of toxin inhibition and transcriptional repression by *Escherichia coli* DinJ–YafQ. *J Biol Chem* 2014;**289**:20559–69. https://doi.org/10.1074/jbc.M114.573006
26. Schureck MA, Maehigashi T, Miles SJ *et al.* Structure of the *Proteus vulgaris* HigB–(HigA)2–HigB toxin–antitoxin complex. *J Biol Chem* 2014;**289**:1060–70. https://doi.org/10.1074/jbc.M113.512095
27. Turnbull KJ, Gerdes K. HicA toxin of *Escherichia coli* derepresses hicAB transcription to selectively produce HicB antitoxin. *Mol Microbiol* 2017;**104**:781–92. https://doi.org/10.1111/mmi.13662
28. Madl T, Van Melderen L, Mine N *et al.* Structural basis for nucleic acid and toxin recognition of the bacterial antitoxin CcdA. *J Mol Biol* 2006;**364**:170–85. https://doi.org/10.1016/j.jmb.2006.08.082
29. Boggild A, Sofos N, Andersen KR *et al.* The crystal structure of the intact *E. coli* RelBE toxin–antitoxin complex provides the structural basis for conditional cooperativity. *Structure* 2012;**20**:1641–8. https://doi.org/10.1016/j.str.2012.08.017
30. Garcia-Pino A, Balasubramanian S, Wyns L *et al.* Allostery and intrinsic disorder mediate transcription regulation by conditional cooperativity. *Cell* 2010;**142**:101–11. https://doi.org/10.1016/j.cell.2010.05.039
31. Dienemann C, Boggild A, Winther KS *et al.* Crystal structure of the VapBC toxin–antitoxin complex from *Shigella flexneri* reveals a hetero-octameric DNA-binding assembly. *J Mol Biol* 2011;**414**:713–22. https://doi.org/10.1016/j.jmb.2011.10.024
32. Brown BL, Grigoriu S, Kim Y *et al.* Three dimensional structure of the MqsR:MqsA complex: a novel TA pair comprised of a toxin homologous to RelE and an antitoxin with unique properties. *PLoS Pathog* 2009;**5**:e1000706. https://doi.org/10.1371/journal.ppat.1000706
33. Schumacher MA, Piro KM, Xu W *et al.* Molecular mechanisms of HipA-mediated multidrug tolerance and its neutralization by HipB. *Science* 2009;**323**:396–401. https://doi.org/10.1126/science.1163806
34. Magnuson R, Lehnherr H, Mukhopadhyay G *et al.* Autoregulation of the plasmid addiction operon of bacteriophage P1. *J Biol Chem* 1996;**271**:18705–10. https://doi.org/10.1074/jbc.271.31.18705
35. Brzozowska I, Zielenkiewicz U. Regulation of toxin–antitoxin systems by proteolysis. *Plasmid* 2013;**70**:33–41. https://doi.org/10.1016/j.plasmid.2013.01.007
36. Talavera A, Tamman H, Ainelo A *et al.* A dual role in regulation and toxicity for the disordered N-terminus of the toxin GraT. *Nat Commun* 2019;**10**:972. https://doi.org/10.1038/s41467-019-08865-z
37. Terawaki Y, Takayasu H, Akiba T. Thermosensitive replication of a kanamycin resistance factor. *J Bacteriol* 1967;**94**:687–90. https://doi.org/10.1128/jb.94.3.687-690.1967
38. Tian QB, Ohnishi M, Tabuchi A *et al.* A new plasmid-encoded proteic killer gene system: cloning, sequencing, and analyzing hig locus of plasmid Rts1. *Biochem Biophys Res Commun* 1996;**220**:280–4. https://doi.org/10.1006/bbrc.1996.0396
39. Pedersen K, Zavialov AV, Pavlov MY *et al.* The bacterial toxin RelE displays codon-specific cleavage of mRNAs in the ribosomal A site. *Cell* 2003;**112**:131–40. https://doi.org/10.1016/S0092-8674(02)01248-5
40. Hurley JM, Woychik NA. Bacterial toxin HigB associates with ribosomes and mediates translation-dependent mRNA cleavage at A-rich sites. *J Biol Chem* 2009;**284**:18605–13. https://doi.org/10.1074/jbc.M109.008763
41. Schureck MA, Dunkle JA, Maehigashi T *et al.* Defining the mRNA recognition signature of a bacterial toxin protein. *Proc Natl Acad Sci USA* 2015;**112**:13862–7. https://doi.org/10.1073/pnas.1512959112
42. Schureck MA, Maehigashi T, Miles SJ *et al.* mRNA bound to the 30S subunit is a HigB toxin substrate. *RNA* 2016;**22**:1261–70. https://doi.org/10.1261/rna.056218.116
43. Tamman H, Ainelo A, Ainsaar K *et al.* A moderate toxin, GraT, modulates growth rate and stress tolerance of Pseudomonas putida. *J Bacteriol* 2014;**196**:157–69. https://doi.org/10.1128/JB.00851-13
44. Hadzi S, Garcia-Pino A, Haesaerts S *et al.* Ribosome-dependent *vibrio cholerae* mRNAse $HigB_2$ is regulated by a beta-strand sliding mechanism. *Nucleic Acids Res* 2017;**45**:4972–83. https://doi.org/10.1093/nar/gkx138
45. Xu BS, Liu M, Zhou K *et al.* Conformational changes of antitoxin HigA from *Escherichia coli* str. K-12 upon binding of its cognate toxin HigB reveal a new regulation mechanism in toxin–antitoxin systems. *Biochem Biophys Res Commun* 2019;**514**:37–43. https://doi.org/10.1016/j.bbrc.2019.04.061
46. Hadzi S, Zivic Z, Kovacic M *et al.* Fuzzy recognition by the prokaryotic transcription factor $HigA_2$ from *Vibrio cholerae*. *Nat Commun* 2024;**15**:3105. https://doi.org/10.1038/s41467-024-47296-3
47. Schureck MA, Meisner J, Hoffer ED *et al.* Structural basis of transcriptional regulation by the HigA antitoxin. *Mol Microbiol* 2019;**111**:1449–62. https://doi.org/10.1111/mmi.14229
48. Datsenko KA, Wanner BL. One-step inactivation of chromosomal genes in *Escherichia coli* K-12 using PCR products. *Proc Natl Acad Sci USA* 2000;**97**:6640–5. https://doi.org/10.1073/pnas.120163297
49. Schureck MA, Repack A, Miles SJ *et al.* Mechanism of endonuclease cleavage by the HigB toxin. *Nucleic Acids Res* 2016;**44**:7944–53. https://doi.org/10.1093/nar/gkw598
50. Kabsch W. XDS. *Acta Crystallogr D Biol Crystallogr* 2010;**66**:125–32. https://doi.org/10.1107/S0907444909047337
51. Adams PD, Afonine PV, Bunkoczi G *et al.* PHENIX: a comprehensive Python-based system for macromolecular structure solution. *Acta Crystallogr D Biol Crystallogr* 2010;**66**:213–21. https://doi.org/10.1107/S0907444909052925
52. Emsley P, Lohkamp B, Scott WG *et al.* Features and development of Coot. *Acta Crystallogr D Biol Crystallogr* 2010;**66**:486–501. https://doi.org/10.1107/S0907444910007493
53. Case DA, I.Y.B.-S.I.Y.B.-S., Brozell SR, Cerutti DS *et al.* University of California, San Francisco, 2018. https://ambermd.org/doc12/Amber18.pdf
54. Maier JA, Martinez C, Kasavajhala K *et al.* ff14SB: improving the accuracy of protein side chain and backbone parameters from ff99SB. *J Chem Theory Comput* 2015;**11**:3696–713. https://doi.org/10.1021/acs.jctc.5b00255

55. Galindo-Murillo R, Robertson JC, Zgarbova M *et al.* Assessing the current state of Amber force field modifications for DNA. *J Chem Theory Comput* 2016;**12**:4114–27. https://doi.org/10.1021/acs.jctc.6b00186
56. Jorgensen WL, Chandrasekhar J, Madura JD *et al.* Comparison of simple potential functions for simulating liquid water. *J Chem Phys* 1983;**79**:926–35. https://doi.org/10.1063/1.445869
57. Salomon-Ferrer R, Gotz AW, Poole D *et al.* Routine microsecond molecular dynamics simulations with AMBER on GPUs. 2. Explicit solvent particle mesh Ewald. *J Chem Theory Comput* 2013;**9**:3878–88. https://doi.org/10.1021/ct400314y
58. Le Grand S, Gotz AW, Walker RC. SPFP: speed without compromise—a mixed precision model for GPU accelerated molecular dynamics simulations. *Comput Phys Commun* 2013;**184**:374–80. https://doi.org/10.1016/j.cpc.2012.09.022
59. Ryckaert JCG, Berendsen HJC. Numerical integration of the cartesian equations of motion of a system with constraints: molecular dynamics of *n*-alkanes. *J Comput Phys* 1977;**23**:327–41. https://doi.org/10.1016/0021-9991(77)90098-5
60. Roe DR, Cheatham TE 3rd. PTRAJ and CPPTRAJ: software for processing and analysis of molecular dynamics trajectory data. *J Chem Theory Comput* 2013;**9**:3084–95. https://doi.org/10.1021/ct400341p
61. Tian QB, Ohnishi M, Murata T *et al.* Specific protein–DNA and protein–protein interaction in the hig gene system, a plasmid-borne proteic killer gene system of plasmid Rts1. *Plasmid* 2001;**45**:63–74. https://doi.org/10.1006/plas.2000.1506
62. Dao-Thi MH, Van Melderen L, De Genst E *et al.* Molecular basis of gyrase poisoning by the addiction toxin CcdB. *J Mol Biol* 2005;**348**:1091–102. https://doi.org/10.1016/j.jmb.2005.03.049
63. Khoo SK, Loll B, Chan WT *et al.* Molecular and structural characterization of the PezAT chromosomal toxin–antitoxin system of the human pathogen *Streptococcus pneumoniae*. *J Biol Chem* 2007;**282**:19606–18. https://doi.org/10.1074/jbc.M701703200
64. Overgaard M, Borch J, Gerdes K. RelB and RelE of *Escherichia coli* form a tight complex that represses transcription via the ribbon–helix–helix motif in RelB. *J Mol Biol* 2009;**394**:183–96. https://doi.org/10.1016/j.jmb.2009.09.006
65. Grabe GJ, Giorgio RT, Hall AMJ *et al.* Auxiliary interfaces support the evolution of specific toxin–antitoxin pairing. *Nat Chem Biol* 2021;**17**:1296–304. https://doi.org/10.1038/s41589-021-00862-y
66. Monti MC, Hernandez-Arriaga AM, Kamphuis MB *et al.* Interactions of Kid-Kis toxin–antitoxin complexes with the parD operator–promoter region of plasmid R1 are piloted by the Kis antitoxin and tuned by the stoichiometry of Kid–Kis oligomers. *Nucleic Acids Res* 2007;**35**:1737–49. https://doi.org/10.1093/nar/gkm073

Received: September 30, 2024. **Revised:** May 21, 2025. **Editorial Decision:** June 5, 2025. **Accepted:** June 23, 2025